DIGITAL ACCESS TO SCHOLARSHIP AT HARVARD
DASH.HARVARD.EDU

HARVARD LIBRARY
Office for Scholarly Communication

Nanoanalytical Analysis of Bisphosphonate-Induced Alterations of Microcalcifications Using a 3D Hydrogel Platform

Citation

Ruiz, Jessica. 2018. Nanoanalytical Analysis of Bisphosphonate-Induced Alterations of Microcalcifications Using a 3D Hydrogel Platform. Doctoral dissertation, Harvard Medical School.

Permanent link

http://nrs.harvard.edu/urn-3:HUL.InstRepos:36923338

Terms of Use

This article was downloaded from Harvard University's DASH repository, and is made available under the terms and conditions applicable to Other Posted Material, as set forth at http://nrs.harvard.edu/urn-3:HUL.InstRepos:dash.current.terms-of-use#LAA

Share Your Story

The Harvard community has made this article openly available.
Please share how this access benefits you. Submit a story .

Accessibility

Table of Contents

Abstract 3
Introduction 4
Methods 7
Results 13
Discussion 16
Conclusions 21
Summary 21
References 22
Figure captions 26
Figures 28

Abstract

Vascular calcification predicts atherosclerotic plaque rupture and cardiovascular events. Retrospective studies of women taking bisphosphonates (BiPs), a proposed therapy for vascular calcification, showed that BiPs paradoxically increased cardiovascular morbidity in patients with prior acute events, but decreased morbidity in event-free patients. We recently demonstrated that calcifying extracellular vesicles (EVs) released by cells within atherosclerotic plaques aggregate and nucleate calcific mineral. We hypothesize that BiPs block EV aggregation and modify existing mineral growth, potentially altering microcalcification morphology and the resultant risk of plaque rupture. 3D collagen hydrogels incubated with calcifying EV mimicked fibrous cap calcification, serving as a platform to image mineral nucleation and test potential therapies for vascular calcification. This study visualized EV aggregation and formation of stress-inducing microcalcifications at single-EV resolution, via scanning electron microscopy (SEM) and atomic force microscopy (AFM). Finite element analysis (FEA) of a representative microcalcification formed in the 3D platform predicted a consequential 350% increase in fibrous cap tensile stress (Figure, red color). Energy-dispersive x-ray spectroscopy (EDS) confirmed that EV aggregates contained calcium and phosphorous. BiP (ibandronate) treatment added on day 0 significantly decreased the size (21.5 μm^2 vs. 14.2 μm^2, $p=0.012$) and amount of EDS-detected calcium (4.32% by weight (wt%) vs. 2.36 wt%, $p<0.001$) and phosphorous (4.26 wt% vs. 1.94 wt%, $p<0.001$) comprising EV aggregates measured on day 8. However, an increase in mineral was measured when BiP was added at later time points (day 6, $n=2$). Mineral composition and morphology, measured with Fourier-transform infrared spectroscopy (FTIR), SEM and AFM, varied depending on the timing of BiP treatment, suggesting that BiP treatment altered microcalcification morphology and composition in a time-dependent manner. These findings support our hypothesis that BiP alter EV-driven calcification, which may help explain confounding clinical data. The study also confirmed that our 3D hydrogel is a viable platform to study EV-mediated mineral nucleation and evaluate potential therapies for cardiovascular calcification.

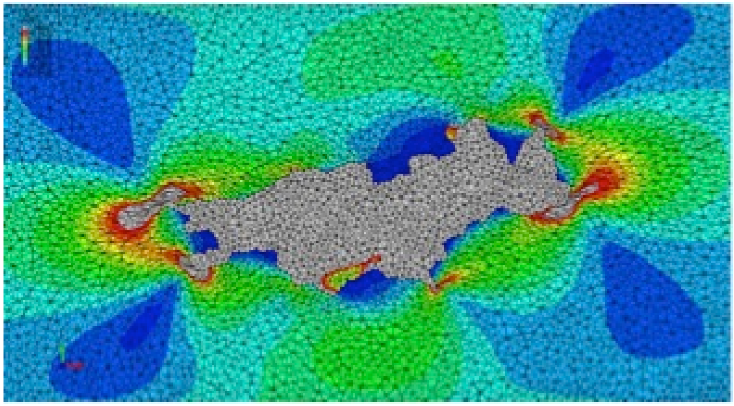

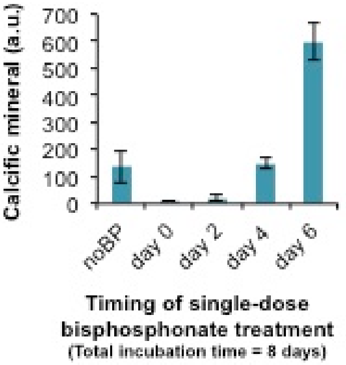
Calcific mineral (a.u.)
700
600
500
400
300
200
100
0
noBP
day 0
day 2
day 4
day 6
Timing of single-dose bisphosphonate treatment
(Total incubation time = 8 days)

Introduction

Atherosclerotic plaque rupture is the leading cause of myocardial infarction and stroke (1) (2). Atheroma-associated calcification was previously thought to be protective against plaque rupture. Recently, however, computed tomography (CT)-derived calcium scores have been formulated to quantify the patient-specific burden of coronary artery calcification. Assessing the correlation between calcium scores and cardiovascular events has demonstrated a predictive power that is superior to and independent from that of lipid scores (3) (4). Clinical cardiovascular risk assessments are more accurate with the inclusion of calcium scores (5, 6). Additionally, clinical studies of vascular calcification, utilizing CT (7) and ultrasound (8), have revealed that the risk of plaque rupture is further heightened with the specific presence of small, 'spotty' calcifications or microcalcifications. A prospective analysis based on the Multi-Ethnic Study of Atherosclerosis (MESA) trial further demonstrated that cardiovascular risk was inversely correlated with the size of calcific deposits associated with atherosclerotic lesions, quantified as a calcium density score (9).

Computational modeling has corroborated the hypothesis that cardiovascular risk is specifically associated with the presence of microcalcifications within the fibrous cap. Due to their size, microcalcifications, ranging from 5μm -15μm in diameter, uniquely mediate an increase in mechanical stress of the surrounding tissue (10-12). This stress amplification occurs due to a mismatch in density between the hard calcifications and the relatively soft, collagen-rich fibrous cap (13). *In silico* modeling has revealed additional variables predicted to modulate biomechanical stress, including microcalcification size, morphology, the presence of neighboring calcifications, and surrounding collagen content (10, 11). Conversely, large calcifications form from the fusion and expansion of several microcalcifications beneath the fibrous cap (14), where they act to reinforce the cap against mechanical deformation as the vessel cycles between systolic and diastolic pressures (15-18). Thus, while the formation of microcalcifications may precede the formation of more stable large calcifications, throughout this process new, potentially plaque-destabilizing microcalcifications are continuously forming.

Histologic studies have revealed the presence of cell-derived vesicles within calcifying atherosclerotic lesions (19-21). Just as bone formation is hypothesized to be an active, cell-driven process (22, 23), mediated by calcifying matrix vesicles, atheroma-associated calcification may similarly be initiated by the production and aggregation of calcifying extracellular vesicles (EV) (12, 14, 24-27). The inflammatory environment of the atherosclerotic lesion can induce the transformation of vascular smooth muscle cells (vSMCs) to an osteochondrogenic phenotype (28-30). Macrophages can also release pro-calcifying vesicles (26). In both processes, specialized vesicles are released, containing the appropriate phospholipids (31-33), ion channels (24, 34) and membrane-associated enzymes (35, 36) to concentrate calcium and phosphate ions within the vesicle and initiate mineral formation (12, 37).

Studying the formation and alteration of EV-nucleated microcalcifications *in vivo* is notoriously difficult, as the size of EVs and microcalcifications lies below the resolution of standard imaging modalities, which is a major barrier to progress in the field. A recent study from Hutcheson et al. was the first to visualize EVs in the initial stages of aggregation and mineral formation, using super-resolution, structured illumination microscopy (14). The current study is an expansion of that work, utilizing a novel, 3D collagen hydrogel system that recapitulates the atherosclerotic fibrous cap and serves as a platform within which EVs can diffuse, aggregate and nucleate microcalcifications. The platform was adapted for high-resolution imaging techniques, and utilized to evaluate a potential pharmacologic therapy for vascular calcification.

One proposed strategy for halting pathologic calcification has been the use of bisphosphonates (BiPs). BiPs were synthesized to mimic pyrophosphate, a compound that was originally isolated from plasma and urine, and identified as an inhibitor of calcium phosphate precipitation and ectopic calcification (38). BiPs are analogs of pyrophosphate, distinguished by a central carbon atom, as opposed to a central oxygen atom, that confers resistance to enzymatic hydrolysis (39). Thus, BiPs inhibit calcification via its physicochemical properties, namely by blocking calcium and phosphate ions from forming crystals, preventing crystal aggregation, and preventing mineral transformation from amorphous calcium phosphate to hydroxyapatite (39). A second, distinct property of BiPs is the ability to inhibit bone resorption, via cell-mediated mechanisms. The biological activity of BiPs is largely directed against osteoclasts, leading to decreased osteoclast recruitment, impaired adhesion, inhibited activity and reduced lifespan (39). As a result, the overall mineral content of bone is increased with BiP treatment, making this an effective treatment option for patients with osteoporosis or other disorders of bone turnover.

In vivo investigations have been performed to explore the physicochemical properties of BiPs, including their ability to inhibit cardiovascular calcification. Studies of first-generation BiPs revealed that the doses required to inhibit cardiovascular calcification also critically compromised normal bone mineralization (39, 40). However, newer, nitrogen-containing BiPs effectively arrested cardiovascular calcification in animal models at doses that did not compromise bone formation (40). Further, BiP treatment has been shown to inhibit calcification of explanted rat aortas, indicating that BiPs can act directly on vascular tissue, independent of bone metabolism (41).

Retrospective clinical data examining the effect of BiP therapy on cardiovascular calcification has demonstrated conflicting findings and intriguing paradoxes. In the field of calcific aortic valve disease, some analyses demonstrate that BiP treatment attenuates disease progression (42-45), while others do not (46, 47). In women with chronic kidney disease, BiP therapy decreased the mortality risk in patients without history of cardiovascular disease (48), but for those patients with a history of prior cardiovascular events, bisphosphonate therapy was associated with an increased mortality rate (49). Additionally, of the women who participated in the Multi-Ethnic Study of Atherosclerosis (MESA), BiP therapy was correlated with a lower rate of cardiovascular calcification in older patients (> 65 years), but a greater rate in younger patients (<65 years) (45).

Therefore, in this study we used a cell-free, 3D collagen platform to examine the direct effect of ibandronate, a nitrogen-containing BiP, on the EV-directed nucleation and growth of microcalcifications. Understanding the cardiovascular-specific action of BiPs is imperative both for the development of anti-calcific therapeutics and to address potential cardiovascular side effects of BiPs used in clinical settings.

Methods

Cell culture and isolation of extracellular vesicles

Human coronary artery smooth muscle cells (SMCs; PromoCell) were expanded, plated for EV isolation and grown to confluence using Smooth Muscle Cell Growth Medium 2 (5% v/v serum; PromoCell). After reaching confluence, cells were cultured in either a control medium comprised of DMEM plus 10% fetal bovine serum (FBS) and 1% penicillin/streptomycin or calcifying medium comprised of control medium plus 10 nM dexamethasone, 100 μM L-ascorbic acid and 10 mM β-glycerophosphate. The media were exchanged every 48 to 72 hours. After at least 14 days of culture (sufficient time to induce osteogenic differentiation of the SMCs (50)), the media were exchanged for control or calcifying medium containing only 0.1% FBS, to minimize the presence of FBS-derived vesicles in the media. After 24 hours of culture, the conditioned 0.1% FBS media were collected, centrifuged for 10 minutes at 1,000*g* to remove cell debris, and the EV-containing supernatants were stored at -80 ^{o}C. In preparation for vesicle experiments, the conditioned media was thawed and EVs were concentrated, resuspended in the appropriate 0.1% FBS control or calcifying medium and re-concentrated using centrifugal filtration (Millipore Amicon Ultra Centrifugal Filter Unit with membrane nominal molecular weight limit of 3 KDa). The final vesicle concentration was four-times that of the original vesicle concentration in conditioned media.

EV assay for calcification potential

An assay for alkaline phosphatase activity (a key regulatory enzyme of vascular calcification (51)) was used to determine the calcification potential of SMC-isolated EVs (AnaSpec SensoLyte® pNPP Alkaline Phosphatatse Assay Kit). Briefly, EVs contained within 1ml of isolated supernatant were pelleted using ultracentrifugation at 100,000*g* for 40 minutes, and resuspended in a solution of 0.2% Triton® X-100 in the provided assay buffer. Resultant values were normalized against protein content (Thermo Scientific Pierce™ BCA Protein Assay Kit).

EV aggregation and calcification in suspension

Calcifying EVs were concentrated 4x and incubated in eppendorf tubes, 400ul per tube, for 8 days at 37^{o}C. At the assigned time points, 57.1 μL of 0.4 mM ibandronate or water (untreated control) was added to the appropriate tubes.

Nanoparticle-tracking analyses (NTA)

NanoSight LM10 (Malvern Instruments) was used to conduct NTA of EV size and concentration within the baseline media isolates and following experiments investigating EV aggregation and calcification in suspension. Vesicles were diluted 1:7 in phosphate buffered saline (PBS) and injected into the laser-illuminated NanoSight chamber. If the vesicle suspension was 4x concentrated during experiment set-up, then the suspension was diluted 1:28. The diluted sample was continuously injected into the chamber using a syringe pump (Malvern), during which five NTA movies were collected, each 1-minute in duration. The distribution of nanoparticle size and concentration within the sample is determined by an analysis of the Brownian motion of the objects recorded in the NTA movies (52). The camera gain used was 9 and the vesicle detection threshold value used was 2. The size and concentration analyses from each movie were averaged, yielding a representative set of data for each sample.

EV mineralization assay

The mineralization of EVs incubated in suspension was quantified using a fluorescent-based mineral-binding dye (Lonza, OsteoImage). Briefly, EV suspensions were ultracentrifuged (100,000g, 40 minutes, 4 °C), the resultant pellet was resuspended in 200 µL of OsteoImage dye and incubated for 30 minutes at room temperature. The dye was removed via ultracentrifugation and the pellets were washed twice with OsteoImage wash buffer, re-isolating the mineralized contents between washes using ultracentrifugation. The final pellet was resuspended in 100 µL of OsteoImage wash buffer and fluorescent intensity was recorded using a plate reader.

3D collagen hydrogel experiments

Collagen hydrogels were cast onto amino-silanated, round (neuVitro, 12mm diameter), glass coverslips, following an adaptation of a previously established protocol (53). Briefly, 150 µL of 0.1M NaOH was added to each coverslip, and the coverslip with solution was heated on a hotplate at 80 °C until the liquid evaporated. Then, the coverslips were removed from the hotplate and 6 drops of (3-aminopropyl)triethoxysilane (APES) was added to the NaOH-treated surface of each. The APES was allowed 5 minutes to react, after which the coverslips were rinsed under a stream of deionized (DI) water. The coverslips were then each transferred to individual wells of a 24 well-plate, and washed twice with DI water, 5 minutes per wash. The second wash solution was exchanged for 0.5% glutaraldehyde in PBS, which was allowed to stand at room temperature for 30 minutes. The coverslips were removed from the glutaraldehyde solution, allowed to air-dry and UV sterilized in a cell culture hood for 30 minutes.

The sterile, amino-silanated coverslips were immediately covered with 75 µL of a 5% solution of rat tail high concentration collagen type I (Corning) in 0.1% FBS calcifying medium. In preparing the collagen solution, the pH was slowly raised to 7-8. The gels were allowed to set for 1 hour at 37 ^{o}C. Calcifying EVs, isolated and four-times concentrated as described above, were then added to each gel, 400 µL per gel. The gels were incubated at 37 ^{o}C for the designated duration of each experiment. At the indicated time points, 57.1 µL of 0.4 mM ibandronate in water (Sigma-Aldrich) or water (untreated control) was added to the appropriate gels (final concentration of ibandronate was 0.05mM). At the end of each experiment, the coverslip-adhered hydrogels were further processed for imaging, as described below.

Scanning electron microscopy (SEM) - sample preparation and imaging

Following incubation with calcifying EVs, as described above, coverslip-adhered collagen hydrogels were immersed in 2% gluataraldehyde in 0.1M sodium cacodylate buffer, pH 7.2, and fixed for 1 hour. The fixed hydrogels were rinsed three times in 0.1M sodium cacodylate buffer, pH 7.2, for 15 minutes per rinse. The hydrogels were then dehydrated in grades of ethanol (10min each; 35%, 50%, 70%, 80%, 95%, 3x10min 100%).

The dehydrated collagen gels were then subjected to critical point drying (Tousimis 931 GL), a process that maintains the structural integrity of a once hydrated sample by exchanging ethanol for liquid carbon dioxide before drying. The dried collagen gels, still adhered to glass coverslips, were mounted onto aluminum stubs (Electron Microscopy Sciences, EMS) using 12mm diameter carbon adhesive tabs (EMS). The mounted collagen gels were sputter coated (EMS 300T D Dual Head sputter coater) with 5 nm of 80:20 platinum:palladium. The uncoated edges of each sample were covered with silver adhesive (EMS), and allowed to dry for at least 30 minutes before imaging.

Samples were imaged in a Supra55VP FESEM (Zeiss) using a secondary electron in-lens detector, 6.4 mm working-distance, and 8.00 kV beam voltage.

Elemental analysis

Energy-dispersive x-ray spectroscopy (EDS) was used to evaluate the elemental composition of microcalcifications generated in 3D collagen hydrogels. The EDS system was connected to the microscope used for SEM, and the same samples were used for SEM and EDS. EDS measurements were taken with a beam energy of 8 kV.

Transmission Electron Microscopy (TEM) – sample preparation and imaging

Collagen hydrogels for TEM were prepared as described above but cast in chambered coverglass wells (LAB-TEK, no. 1.5 borosilicate), 300 μL per well. Calcifying EVs were concentrated 7.5x and added to each gel, along with a suspension of ibandronate or water, such that the total volume added to each gel was 250 μL and the final concentration of ibandronate was 0.05 mM. Samples were fixed for at least 2 hours at room temperature in 2.5% glutaraldehyde/ 2% paraformaldehyde in 0.1 M sodium cacodylate buffer, pH 7.4. The samples were washed in 0.1 M cacodylate buffer and postfixed with 1% osmiumtetroxide (OsO4)/1.5% potassiumferrocyanide (KFeCN6) for 1 hour, washed in water 3x and incubated in 1% aqueous uranyl acetate for 1hr followed by 2 washes in water and subsequent dehydration in grades of alcohol (10 minutes each; 50%, 70%, 90%, 2x10min 100%). The samples were then put in propyleneoxide for 1 hour and infiltrated overnight in a 1:1 mixture of propyleneoxide and TAAB Epon (Marivac Canada Inc. St. Laurent, Canada). The following day the samples were embedded in TAAB Epon and polymerized at 60^{o}C for 48 hours.

Ultrathin sections (about 80 nm) were cut on a Reichert Ultracut-S microtome, picked up on to copper grids stained with lead citrate and examined in a JEOL 1200EX Transmission electron microscope, images were recorded with an AMT 2k CCD camera.

Fourier-transform infrared spectroscopy (FTIR)

Fourier transform infrared spectroscopy (Bruker, FTIR) was used to perform elemental analyses of microcalcifications formed from EVs incubated with calcifying medium in suspension. The FTIR set-up was comprised of a motorized stage and polarized optical microscope. The microscope assisted in identifying regions to analyze. Attenuated total reflectance mode (single bounce Ge crystal) was used to collect spectral data in a range from 4,000 to 600 cm^{-1}.

Confocal microscopy

Confocal microscopy was used to quantify the size and number of microcalcifications formed in the 3D collagen hydrogel experiments. One day before sample collection and imaging, a near-infrared calcium tracer (OsteoSense 680, Perkin Elmer) was added to the hydrogel containing well and incubated at 37 °C. The following day, the coverslip-adhered hydrogels were mounted onto glass slides using SHUR/*Mount*™ (TBS). Continuous-wave confocal microscopy (Nikon A1) was used to collect fluorescent images of the gels. Five sets of z-stack optical sections were collected per gel, with the height of each stack selected to encompass the entire fluorescent signal present within that region of the gel.

An algorithm was custom-written (MATLAB) to count the number of microcalcifications imaged in the z-stacks and to calculate the volume of each identified microcalcification. Each z-stack was converted from grayscale to a series of binary images using a threshold that disregarded noise from pixels with a luminance less than 25%. A microcalcification was defined as a three-dimensional region containing 26 or more connected pixels that were positive for the fluorescent calcium tracer, after applying the binary threshold.

Multiscale Finite Element Analysis (FEA)

(Collaboration with Prof. Sheldon Weinbaum and Dr. Luis Cardoso; City College of NY, the entire FEA protocol was carried out by these collaborators)

The stress concentration created by microcalcifications treated with a single dose of bisphosphonate on day 2, 4 or 6 of incubation, or untreated microcalcifications, was computed using a multiscale finite element analysis in ABAQUS (version 6.14.3, Simulia, Providence, RI). A global finite element (FE) model and three submodels were prepared to obtain the stress concentration factor (SCF) produced by the presence of a single microcalcification. For the global model, a 3D FE volumetric tetrahedral mesh was created, depicting the soft tissue, lipid and cap of the atheroma. Material properties were then assigned using an incompressible neo-Hookean isotropic hyperelastic model. In this model, the strain energy function is W =C(I1 - 3), where C is a material constant, such that the initial Young's modulus E = 6 x C, and I1 is the first invariant of the strain tensor. 120 mmHg were applied as hydrostatic load on the lumen of the artery, deforming the artery and creating a tensile stress in the fibrous cap. Stresses and strains were recorded at each node. The first-level submodel consisted of the whole cap, in which the results from the global model drive the boundary conditions, with the difference that the 3D mesh of the cap was refined, with much smaller size finite elements. The second-level submodeling consisted of a segment of the cap, in which the size of the finite elements were again reduced, to obtain a much more accurate stress and strain 3D distribution maps. In the third-level submodel, a smaller region of interest of the cap, 20x20x20 μm size was prepared, in which the SEM-based microcalcifications were included. The material properties of the cap remained the same, but the regions corresponding to the microcalcifications from SEM were assigned linear elastic material properties corresponding to calcified tissue (10 GPa). The results from the previous submodel level were used to drive the boundary conditions of this submodel. A 3D map of stresses and strains was obtained for each one of the SEM-based FE models of microcalcifications. Control tests were performed following the approach described above, with the difference that the 3D volume occupied by the microcalcifications was replaced by soft tissue, with the same hyperelastic properties as the cap. Stress concentration was calculated as the ratio of the stresses with and without microcalcifications and measured in triplicate per time point.

Atomic Force Microscopy (AFM) – sample reparation and imaging

(Collaboration with Prof. Paolo Bergese, Sara Busatto, and Stefania Federici, University of Bresica, the entire AFM protocol was carried out by these collaborators)

Samples containing microcalcifications were resuspended in 100 μL sterile MilliQ water added with protease inhibitor 1:1000. 4-6 μL of sample were then spotted onto freshly cleaved mica sheets (Grade V-1, thickness 0.15 mm, size 15x15 mm^2). The samples were then incubated at 30°C for 20 minutes over a heating plate to let the sample droplet dry. They were finally imaged with a NaioAFM (Nanosurf AG) equipped with Multi75Al-G probe (Budget Sensors, Sofia, Bulgaria). Images were acquired in tapping mode, with a scan size ranging from 2 μm to 25 μm and a scan speed from 0.8 s to 1.0 s per scanning line. The imaging analysis of the deposited microcalcifications was performed with the software WSxM 5.0 image (54), AFM topography 5 μm x 5 μm images were used.

Statistical analyses

Error bars represent standard deviation. The variable n represents the number of individual experiments performed. Quantitative data was analyzed for statistical significance using a Student’s T-test (Microsoft Excel) if comparing two groups, or a one-way ANOVA with Tukey’s Multiple Comparison’s Test (GraphPad Prism) if comparing multiple groups. Significance was defined as $p < 0.05$.

Results

3D collagen hydrogels were incubated with calcifying EVs for 8 days (Fig. 1*A*). The formation of microcalcifications within the 3D platform was validated using multiple imaging modalities (Fig. 1 *B*-*F*). Scanning electron microscopy (SEM) revealed the aggregation of EVs along and between collagen fibrils (Fig. 1*B* and *C*). The EV-aggregates formed *in vitro* resembled aggregates of dense, spherical particles visualized within the calcific region of a human atherosclerotic plaque, using density-dependent colorimetric SEM (DDC-SEM) (55) (Fig. 1*D*). Using transmission electron microscopy (TEM), similar, rough appearing vesicular structures were identified in sections of EV-incubated hydrogels and in human atherosclerotic tissue (Fig. 1*E* and *F,* respectively). Confocal microscopy of collagen hydrogels stained with a fluorescent calcium tracer confirmed that incubation with calcifying EVs leads to microcalcification formation (Fig. 2*A*). Energy dispersive spectroscopy (EDS), a technique used to analyze elemental composition, concurrent with SEM, demonstrated that EV-aggregates formed in our 3D platform contained phosphorous and calcium (Fig. 2*B*). EDS mapping of EV-aggregates (Fig. 2*C*) further visualized the phosphorous (Fig. 2*D*) and calcium (Fig. 2*E*) content of these structures.

Multiscale finite element analysis (FEA) was used to analyze the tissue stress that would be associated with the microcalcifications formed in our 3D platform. A collaborator at the City College of New York performed all FEA. The multiscale FEA provides the circumferential stresses at three scale lengths in a 3D volumetric tetrahedral mesh representing the soft tissue, lipid and fibrous cap components of an atheroma. The stresses in the whole atheroma are used to compute the stresses in the cap with much higher resolution, and then in a much smaller region of interest within the cap containing a single microcalcification (56). Each submodel comprises between 1-3 million tetrahedral elements, and the dimension of the finite elements used in the last submodel is smaller than 50 nm. A representative microcalcification formed in the 3D platform was selected (Fig. 3*A*) and virtually inserted into the fibrous cap of the simulated atheroma. To conduct a baseline calculation, this microcalcification structure was first assigned ‘soft’ material properties similar to fibrous cap, and FEA predicted a negligible increase in fibrous cap tensile stress (Fig. 3*B* – blue color). However, when the microcalcification structure was assigned ‘hard’ material properties of mineral, FEA predicted a 350% increase in fibrous cap tensile stress (stress concentration factor, or SCF) due to the presence of this single microcalcification (Fig. 3*C* and *D* – red color).

To investigate the effect of BiP treatment on the formation and growth of EV-nucleated microcalcifications, a single dose of the BiP ibandronate was simultaneously added with calcifying EVs to the 3D collagen system. After 8 days of incubation, SEM images demonstrated that, as compared to untreated samples (Fig. 4*A* and *C*), BiP treatment on day 0 reduced the maximum size of microcalcifications formed in the 3D system (Fig. 4*B* and *D*). A custom image analysis algorithm confirmed the decrease in microcalcification size with BiP treatment at the start of the experiment (21.5 μm^2 vs. 14.2 μm^2, $p = 0.012$). EDS further indicated that BiP treatment altered the elemental composition of microcalcifications, with a decrease in both calcium (4.32% by weight (wt%) vs. 2.36 wt%, $p<0.001$) and phosphorous (4.26 wt% vs. 1.94 wt%, $p<0.001$).

We next examined the time-dependent effect of BiP treatment on microcalcification formation (Fig. 5*A*). Calcifying EVs were incubated in osteogenic medium for 8 days. Each sample received a single-dose of BiP, but the time at which the BiP was added varied. The single-dose of BiP was added either on day 0, like before, or 2, 4 or 6 days after the experiment started. All samples were collected on day 8. Using a fluorescent-based assay, the amount of calcific mineral detected on day 8 was significantly decreased for samples treated with BiP on day 0 or day 2, as compared to untreated samples (Fig. 5*B*). Treatment on day 4 did not alter the amount of mineral detected on day 8, and treatment on day 6 significantly increased the amount of calcific mineral measured (Fig. 5*B*).

BiP-treated microcalcifications were next imaged using two techniques, SEM and atomic force microscopy (AFM). All AFM data was collected by collaborators at the University of Brescia. This imaging further revealed that BiP treatment altered microcalcification morphology in a time-dependent manner (Fig. 6). While untreated microcalcifications were imaged as orderly, elongated clusters of rough, spherical structures ranging from 100-200 nm in diameter (Fig. 6*A*), BiP-treated microcalcifications were arrangements of <30 nm particles (Fig. 6*B*). These particles formed spherical aggregates in the samples that underwent early (day 2) BiP treatment (Fig. 6*B*), with smaller spherical regions of increased mineral thickness captured by AFM (Fig. 6*F* – bright orange). BiP treatment on day 4 resulted in microcalcifications that were also composed of small particles (Fig. 6*C*), but with a height roughly equivalent to that of untreated microcalcifications (Fig. 6*G* vs *E* – bright orange). Late BiP treatment on day 6 resulted in microcalcifications with a less-ordered structure (Fig. 6*D*), composed of sheet-like regions interrupted by several gaps (Fig. 6*D* and *H*). Further, day 6 treated microcalcifications had one-fifth of the height of untreated microcalcifications, as measured by AFM (Fig. 6*H* vs Fig. 6*E*).

Fourier-transform infrared spectroscopy (FTIR) indicated that the chemical composition of the analyzed microcalcifications was altered following BiP treatment (Fig. 7*A*). Compared to the untreated group, the BiP-treated samples demonstrated a spectral peak or prominent shoulder at 1120 cm^{-1}, as well as an alteration in the morphology of the peak at 1080 cm^{-1} and the spectral slope between the peaks at 980 cm^{-1} and 1080 cm^{-1}. FEA was again used to estimate the tissue stress associated with BiP-treated versus untreated microcalcifications. There was no statistical difference between the SCF that was predicted for microcalcifications that were not treated with BiP (Fig. 8*A*, *E*), versus those that did undergo single-dose BiP treatment on incubation day 2, 4 or 6 (Fig. 8*B*-*E*. p=0.473, p=0.552, p=0.716, respectively).

Discussion

In this study, a 3D collagen hydrogel platform was used for the first time to examine EV-mediated microcalcifications and morphological and chemical alterations consequential to targeted therapy. Through analyses with SEM, TEM and confocal microscopy, we confirmed that the 3D platform is compatible with multiple, high-resolution imaging modalities and could be potentially used for a high throughput screening for drug development. High-resolution imaging allows for detailed analysis of the initial stages of microcalcification formation, which is particularly difficult to observe due to the nanoscale dimensions of this process. While the reductionist approach of this platform limits the degree to which the results accurately recapitulate microcalcification formation and interaction with the complex *in vivo* environment of an atheroma, the cell-free combination of calcifying EVs and type-I-collagen allowed for a focused investigation of EV-mediated mineral formation and the isolated effect of BiP therapy on that process. Future studies however, should investigate the potential impact of BiP on the cells that produce EVs, and if the calcification potential of EVs is altered by exposure of the parent cells to BiP.

FEA demonstrated that our 3D platform recapitulated the formation of microcalcifications predicted to cause a significant increase in fibrous cap tensile stress (Fig.3). Thus, this platform can be used for the re-creation and analysis of plaque-destabilizing microcalcifications. These studies are of particular clinical interest because only a subset of plaque-associated microcalcifications, identified via high-resolution microcomputed tomography and histological analysis of human tissue, are predicted to increase the risk of plaque rupture (10). Specifically, factors that contribute to an increased risk of plaque rupture include a) the presence of thin regions of the fibrous cap, b) a single microcalcification of diameter 5 μm - 65 μm (11), c) microcalcifications with ellipsoid morphology (56), d) orientation of an ellipsoid microcalcification along the tensile axis of the fibrous cap (56), and e) a pair of microcalcifications aligned along the tensile axis of the fibrous cap and closely spaced together such that the ratio of the distance between the microcalcifications and the microcalcification diameter is <0.4 (10). *In vitro* systems amenable to high-resolution analysis, such as our 3D platform, have the potential to advance our understanding of the conditions and processes that drive the formation of plaque-destabilizing microcalcifications, ultimately informing targeted therapies for vascular calcification.

FEA analysis further revealed that treatment with a single-dose of BiP did not significantly alter the predicted fibrous cap tensile stress attributable to microcalcifications formed using the 3D platform (Fig. 8E). This data suggests that, despite the BiP-induced changes in mineral morphology, composition and overall amount of mineral formed, BiP treatment neither mitigates nor exacerbates the danger that an individual calcification poses to fibrous plaque stability. However, this study was limited in that it did not evaluate the likelihood that microcalcifications will be located in pairs adjacent to one another, which can increase the risk of plaque rupture, as outlined above. Further, the FEA model did not account for changes in microcalcification height, as measured by AFM (Fig. 6*E-F*). Future studies should incorporate microcalcification height and spacing into predictive models, to more accurately estimate the BiP-mediated influence on the overall risk of plaque rupture.

The present study further demonstrated that the effect of BiP treatment on microcalcification formation is dependent on the extent of EV-mineralization at the time BiP is introduced to the system. We previously reported that EV-driven mineral deposition begins after 3 days of incubation in osteogenic medium (14). Here, we demonstrated that one-time treatment of calcifying EVs with BiP on day 0 or after 2 days of incubation resulted in a compelling inhibition of mineral formation measured after 8 days of incubation. Correspondingly, microcalcifications that underwent treatment on day 2 of incubation were found to have altered chemical composition (Fig. 7), altered morphology and reduced mineral height (Fig. 6*B* and *F*). BiP are analogous to pyrophosphate, a natural inhibitor of mineral formation that binds nascent calcium-phosphate crystals and prevents mineral formation (57). The data therefore suggest that BiP treatment has the potential to inhibit vascular calcification, in part via a pyrophosphate-like mechanism, but only if introduced before mineral formation begins. Thus, these findings may help explain the clinical observation that women who initiate BiP therapy without a prior history of cardiovascular events, and therefore a lower likelihood of preexisting vascular calcification, are protected from all-cause mortality (48).

However, BiP treatment added after 4 days of incubation led to no change in the amount of mineral measured 4 days later, but did result in a substantial change in mineral morphology (Fig. 6 *C, G*) and composition (Fig. 7). Treatment following 6 days of incubation dramatically increased the amount of mineral detected 2 days later, and while the chemical composition of this mineral most closely matched the untreated control (Fig. 7), the morphology observed was starkly altered (Fig. 6 *D, H*). Once mineral formation begins, pyrophosphate is expected to bind to and prevent the continued expansion of mineral crystals. In our system, if treatment with BiP following 4 or 6 days of incubation mimicked pyrophosphate, we would expect to see no change in mineral morphology and a reduction in the amount of mineral measured after 8 days of incubation, as compared to the untreated control. Thus, the data indicate that, if BiP treatment is started after microcalcifications have begun to form, the alterations induced by BiP treatment cannot be explained by the pyrophosphate-like properties of BiP alone. This suggests that the physicochemical interplay between BiPs and vascular calcification are more complex, and understanding these interactions may be the key to understanding the paradox of the clinical consequences of BiP treatment.

BiP molecules absorb onto the hydrated surface layer of calcium phosphate mineral through a three-step process. Phosphonate groups interact with calcium ions, which leads to phosphonate deprotonation. These free protons interact with hydrogen phosphate on the mineral surface and $H_2PO_4^-$ ions are released. However, the exchange ratio between BiP and $H_2PO_4^-$ ions varies with mineral composition and maturity, as well as the type of BiP used (58). For non-apatitic mineral, like vascular microcalcifications, the ions comprising the hydrated surface layer are particularly exchangeable (59), which suggests that there may be a greater degree of interaction between BiP and vascular calcifications versus that with bone. Additionally, the larger surface area to volume ratio of microcalcifications relative to bone may mean that alterations within surface layer have a greater effect on material properties of entire structure. Therefore, it is critical that studies of BiP-mineral interactions be conducted with microcalcifications and calcifications that mimic those formed in vascular tissue.

In literature it is acknowledged that BiP adsorption onto mineral crystals may alter crystal growth, size, aggregation (57), all of which regulate the biomechanical properties of calcified tissues (60). While the extent to which BiP adsorption influences mineral properties is poorly understood, it is possible that interactions at different points of mineral maturity differentially alter the structure of the surface layer (58) and possibly mineral integrity (59), both of which likely contribute to the biomechanical properties that directly influence the risk of plaque rupture. Ultimately, if BiP adsorption does indeed alter the biomechanics of how microcalcifications interact with the fibrous cap, this may help explain the second half of the clinical paradox, namely, that women with a preexisting history of cardiovascular events, and therefore preexisting microcalcifications, are at a higher risk of death following the initiation of BiP therapy (49).

BiP activity *in vivo* can be divided into two categories: biological activity that inhibits bone resorption and physicochemical activity that inhibits normal bone mineralization (39). First-generation BiPs, like etidronate, are equally potent in biologic and physicochemical activity. Therefore, the doses of first-generation BiP necessary to prevent bone resorption also result in inhibition of normal bone mineralization (61). In comparison, newer-generation, nitrogen-containing BiPs, such as ibandronate, are 1,000 to 10,000-times more potent inhibitors of bone resorption, without a correlated increase in their inhibition of normal mineral formation (39, 62). Thus, nitrogen-containing BiP are frequently used in clinical practice to inhibit bone resorption in conditions such as osteoporosis, because the low doses required to mitigate bone resorption do not adversely impact normal bone mineralization. Surprisingly, studies of arterial calcification in rats have demonstrated that nitrogen-containing BiPs inhibit arterial calcification at doses analogous to those used in humans to treat osteoporosis, while preserving normal bone mineralization (40). However, it is important to note that each nitrogen-containing BiP has a unique molecular charge, chemical structure and atomic configuration (39, 57). Even subtle changes in this structure lead to differences in mineral-binding affinity and biologic potency (57), which may in turn regulate BiP influence on mineral formation. A limitation to the present study, therefore, is that the findings are specific to consequences of ibandronate treatment. Future studies are needed to characterize the effects of different BiPs on microcalcification formation. It will be important to determine which effects are shared among all BiPs and which are BiP-specific.

Calcification plays a key role in determining the stability of an atherosclerotic plaque. Mathematical modeling of fibrous cap biomechanics has revealed that the cap-destabilizing risk of microcalcifications depends on many factors, including size, shape, proximity to other microcalcifications and location within the fibrous cap. A fifth factor that has not been adequately explored in this context is mineral composition. As opposed to physiologic calcification, which occurs through a well-controlled process and results in the uniform deposition of a single type of highly organized, crystalline mineral, pathologic calcification is an active but less controllable and disordered process that results in the formation of one or more types of immature, poorly crystalline and non-apatitic mineral that have proven difficult to characterize (63, 64). Differences in chemical composition and maturity are evident in alterations of crystallite structure and surface properties, which ultimately correspond to differences in biological and structural functionality (65). Microcalcifications destabilize the fibrous cap because of the mismatch in material properties between soft collagen and lipids, and hard, brittle calcium phosphate. More in depth studies are required to obtain a precise understanding of the material properties and chemical characteristics unique to vascular calcific deposits, how BiP treatment alters the properties and morphology of microcalcifications, and how these changes influence the risk of plaque rupture. Our 3D collagen platform is a useful tool to identify vascular calcification-specific properties, and to ultimately screen drugs that manipulate these properties to mitigate cardiovascular risk while minimizing off-target effects on bone.

Conclusions

The 3D collagen platform, mimicking the fibrous cap, allowed for direct visualization and characterization of the formation of EV-nucleated microcalcifications, using multiple high-resolution imaging modalities. BiP did not consistently prevent microcalcification formation, but altered the rate of growth, the morphology and the chemical composition of microcalcifications in a time-dependent manner. Future studies are required to determine the mechanism by which BiPs alter microcalcification morphology and mineral composition, and to further elucidate how these changes impact cardiovascular risk.

Summary

The most common cause of heart attacks or strokes is the rupture of plaques that have grown within blood vessels. Initially, these plaques are formed from soft cholesterol that builds up inside the walls of blood vessels. Over time, small pieces of hard mineral form within these plaques, which destabilize the plaque and make it more likely to rupture. In this project, a three-dimensional platform was designed to study how these pieces of mineral form, using high-powered microscopes. The platform was also used to determine if bisphosphonate therapy, commonly used to treat osteoporosis, could prevent mineral formation. The results showed that bisphosphonates only prevented mineral formation when treatment was started early. When bisphosphonate treatment was started later, a greater amount of mineral formed. Finally, the shape and type of mineral formed differed depending on when the bisphosphonate treatment was given. Overall, more studies are needed to determine how bisphosphonate treatment impacts the process of mineral formation.

References

1. Lloyd-Jones D*, et al.* (2010) Executive summary: heart disease and stroke statistics--2010 update: a report from the American Heart Association. *Circulation* 121(7):948-954.
2. Go AS*, et al.* (2013) Heart disease and stroke statistics--2013 update: a report from the American Heart Association. *Circulation* 127(1):e6-e245.
3. Vliegenthart R*, et al.* (2005) Coronary calcification improves cardiovascular risk prediction in the elderly. *Circulation* 112(4):572-577.
4. Martin SS*, et al.* (2014) Dyslipidemia, coronary artery calcium, and incident atherosclerotic cardiovascular disease: implications for statin therapy from the multi-ethnic study of atherosclerosis. *Circulation* 129(1):77-86.
5. Elkeles RS*, et al.* (2008) Coronary calcium measurement improves prediction of cardiovascular events in asymptomatic patients with type 2 diabetes: the PREDICT study. *Eur Heart J* 29(18):2244-2251.
6. Matsushita K*, et al.* (2015) Subclinical atherosclerosis measures for cardiovascular prediction in CKD. *J Am Soc Nephrol* 26(2):439-447.
7. Ferencik M*, et al.* (2012) A computed tomography-based coronary lesion score to predict acute coronary syndrome among patients with acute chest pain and significant coronary stenosis on coronary computed tomographic angiogram. *Am J Cardiol* 110(2):183-189.
8. Ehara S*, et al.* (2004) Spotty calcification typifies the culprit plaque in patients with acute myocardial infarction: an intravascular ultrasound study. *Circulation* 110(22):3424-3429.
9. Criqui MH*, et al.* (2014) Calcium density of coronary artery plaque and risk of incident cardiovascular events. *JAMA* 311(3):271-278.
10. Kelly-Arnold A*, et al.* (2013) Revised microcalcification hypothesis for fibrous cap rupture in human coronary arteries. *Proceedings of the National Academy of Sciences of the United States of America* 110(26):10741-10746.
11. Maldonado N, Kelly-Arnold A, Cardoso L, & Weinbaum S (2013) The explosive growth of small voids in vulnerable cap rupture; cavitation and interfacial debonding. *J Biomech* 46(2):396-401.
12. Ruiz JL, Weinbaum S, Aikawa E, & Hutcheson JD (2016) Zooming in on the genesis of atherosclerotic plaque microcalcifications. *J Physiol* 594(11):2915-2927.
13. Vengrenyuk Y*, et al.* (2006) A hypothesis for vulnerable plaque rupture due to stress-induced debonding around cellular microcalcifications in thin fibrous caps. *Proceedings of the National Academy of Sciences of the United States of America* 103(40):14678-14683.
14. Hutcheson JD*, et al.* (2016) Genesis and growth of extracellular-vesicle-derived microcalcification in atherosclerotic plaques. *Nat Mater* 15(3):335-343.
15. Maldonado N, Kelly-Arnold A, Laudier D, Weinbaum S, & Cardoso L (2015) Imaging and analysis of microcalcifications and lipid/necrotic core calcification in fibrous cap atheroma. *Int J Cardiovasc Imaging* 31(5):1079-1087.

16. Imoto K, *et al.* (2005) Longitudinal structural determinants of atherosclerotic plaque vulnerability: a computational analysis of stress distribution using vessel models and three-dimensional intravascular ultrasound imaging. *J Am Coll Cardiol* 46(8):1507-1515.
17. Wong KK, Thavornpattanapong P, Cheung SC, Sun Z, & Tu J (2012) Effect of calcification on the mechanical stability of plaque based on a three-dimensional carotid bifurcation model. *BMC Cardiovasc Disord* 12:7.
18. Holzapfel GA, Mulvihill JJ, Cunnane EM, & Walsh MT (2014) Computational approaches for analyzing the mechanics of atherosclerotic plaques: a review. *J Biomech* 47(4):859-869.
19. Kim KM (1976) Calcification of matrix vesicles in human aortic valve and aortic media. *Fed Proc* 35(2):156-162.
20. Tanimura A, McGregor DH, & Anderson HC (1983) Matrix vesicles in atherosclerotic calcification. *Proc Soc Exp Biol Med* 172(2):173-177.
21. Hsu HH & Camacho NP (1999) Isolation of calcifiable vesicles from human atherosclerotic aortas. *Atherosclerosis* 143(2):353-362.
22. Stanford CM, Jacobson PA, Eanes ED, Lembke LA, & Midura RJ (1995) Rapidly forming apatitic mineral in an osteoblastic cell line (UMR 106-01 BSP). *J Biol Chem* 270(16):9420-9428.
23. Drabek K, van de Peppel J, Eijken M, & van Leeuwen JP (2011) GPM6B regulates osteoblast function and induction of mineralization by controlling cytoskeleton and matrix vesicle release. *J Bone Miner Res* 26(9):2045-2051.
24. Anderson HC (2003) Matrix vesicles and calcification. *Curr Rheumatol Rep* 5(3):222-226.
25. Kapustin AN, *et al.* (2011) Calcium regulates key components of vascular smooth muscle cell-derived matrix vesicles to enhance mineralization. *Circ Res* 109(1):e1-12.
26. New SE, *et al.* (2013) Macrophage-derived matrix vesicles: an alternative novel mechanism for microcalcification in atherosclerotic plaques. *Circ Res* 113(1):72-77.
27. Tanimura A, McGregor DH, & Anderson HC (1986) Calcification in atherosclerosis. I. Human studies. *J Exp Pathol* 2(4):261-273.
28. Tintut Y, Patel J, Parhami F, & Demer LL (2000) Tumor necrosis factor-alpha promotes in vitro calcification of vascular cells via the cAMP pathway. *Circulation* 102(21):2636-2642.
29. Aikawa E, *et al.* (2007) Osteogenesis associates with inflammation in early-stage atherosclerosis evaluated by molecular imaging in vivo. *Circulation* 116(24):2841-2850.
30. Demer LL & Tintut Y (2008) Vascular calcification: pathobiology of a multifaceted disease. *Circulation* 117(22):2938-2948.
31. Mebarek S, *et al.* (2013) Phospholipases of mineralization competent cells and matrix vesicles: roles in physiological and pathological mineralizations. *Int J Mol Sci* 14(3):5036-5129.
32. Wu LN, *et al.* (1993) Characterization of the nucleational core complex responsible for mineral induction by growth plate cartilage matrix vesicles. *J Biol Chem* 268(33):25084-25094.

33. Wu LN*, et al.* (1997) Physicochemical characterization of the nucleational core of matrix vesicles. *J Biol Chem* 272(7):4404-4411.
34. Anderson HC, Garimella R, & Tague SE (2005) The role of matrix vesicles in growth plate development and biomineralization. *Front Biosci* 10:822-837.
35. Ciancaglini P*, et al.* (2010) Kinetic analysis of substrate utilization by native and TNAP-, NPP1-, or PHOSPHO1-deficient matrix vesicles. *J Bone Miner Res* 25(4):716-723.
36. Kirsch T, Swoboda B, & Nah H (2000) Activation of annexin II and V expression, terminal differentiation, mineralization and apoptosis in human osteoarthritic cartilage. *Osteoarthritis Cartilage* 8(4):294-302.
37. Hutcheson JD, Maldonado N, & Aikawa E (2014) Small entities with large impact: microcalcifications and atherosclerotic plaque vulnerability. *Curr Opin Lipidol* 25(5):327-332.
38. Fleisch H & Bisaz S (1962) Isolation from urine of pyrophosphate, a calcification inhibitor. *Am J Physiol* 203:671-675.
39. Fleisch H (1998) Bisphosphonates: mechanisms of action. *Endocr Rev* 19(1):80-100.
40. Price PA, Faus SA, & Williamson MK (2001) Bisphosphonates alendronate and ibandronate inhibit artery calcification at doses comparable to those that inhibit bone resorption. *Arterioscler Thromb Vasc Biol* 21(5):817-824.
41. Lomashvili KA, Monier-Faugere MC, Wang X, Malluche HH, & O'Neill WC (2009) Effect of bisphosphonates on vascular calcification and bone metabolism in experimental renal failure. *Kidney Int* 75(6):617-625.
42. Innasimuthu AL & Katz WE (2011) Effect of bisphosphonates on the progression of degenerative aortic stenosis. *Echocardiography* 28(1):1-7.
43. Skolnick AH, Osranek M, Formica P, & Kronzon I (2009) Osteoporosis treatment and progression of aortic stenosis. *Am J Cardiol* 104(1):122-124.
44. Sterbakova G, Vyskocil V, & Linhartova K (2010) Bisphosphonates in calcific aortic stenosis: association with slower progression in mild disease--a pilot retrospective study. *Cardiology* 117(3):184-189.
45. Elmariah S*, et al.* (2010) Bisphosphonate Use and Prevalence of Valvular and Vascular Calcification in Women MESA (The Multi-Ethnic Study of Atherosclerosis). *J Am Coll Cardiol* 56(21):1752-1759.
46. Aksoy O*, et al.* (2012) Do bisphosphonates slow the progression of aortic stenosis? *J Am Coll Cardiol* 59(16):1452-1459.
47. Pawade TA, Newby DE, & Dweck MR (2015) Calcification in Aortic Stenosis: The Skeleton Key. *J Am Coll Cardiol* 66(5):561-577.
48. Hartle JE*, et al.* (2012) Bisphosphonate therapy, death, and cardiovascular events among female patients with CKD: a retrospective cohort study. *Am J Kidney Dis* 59(5):636-644.
49. Perkins RM*, et al.* (2014) Bisphosphonates and mortality in women with CKD and the presence or absence of cardiovascular disease. *Clin J Am Soc Nephrol* 9(5):874-880.
50. Steitz SA*, et al.* (2001) Smooth muscle cell phenotypic transition associated with calcification: upregulation of Cbfa1 and downregulation of smooth muscle lineage markers. *Circ Res* 89(12):1147-1154.

51. Hutcheson JD*, et al.* (2014) Enrichment of calcifying extracellular vesicles using density-based ultracentrifugation protocol. *J Extracell Vesicles* 3:25129.
52. Wright M (2012) Nanoparticle tracking analysis for the multiparameter characterization and counting of nanoparticle suspensions. *Methods Mol Biol* 906:511-524.
53. Tse JRE, A.J. (2010) Preparation of Hydrogel Substrates with Tunable Mechanical Properties. *Curr Protoc Cell Biol* 47:10.16.11-10.16.16.
54. Horcas I*, et al.* (2007) WSXM: a software for scanning probe microscopy and a tool for nanotechnology. *Rev Sci Instrum* 78(1):013705.
55. Bertazzo S*, et al.* (2013) Nano-analytical electron microscopy reveals fundamental insights into human cardiovascular tissue calcification. *Nat Mater* 12(6):576-583.
56. Cardoso L, Kelly-Arnold A, Maldonado N, Laudier D, & Weinbaum S (2014) Effect of tissue properties, shape and orientation of microcalcifications on vulnerable cap stability using different hyperelastic constitutive models. *J Biomech* 47(4):870-877.
57. Russell RG, Watts NB, Ebetino FH, & Rogers MJ (2008) Mechanisms of action of bisphosphonates: similarities and differences and their potential influence on clinical efficacy. *Osteoporos Int* 19(6):733-759.
58. Pascaud P, Gras P, Coppel Y, Rey C, & Sarda S (2013) Interaction between a bisphosphonate, tiludronate, and biomimetic nanocrystalline apatites. *Langmuir* 29(7):2224-2232.
59. Errassifi F*, et al.* (2014) Infrared, Raman and NMR investigations of risedronate adsorption on nanocrystalline apatites. *J Colloid Interface Sci* 420:101-111.
60. Eanes ED & Hailer AW (2000) Anionic effects on the size and shape of apatite crystals grown from physiological solutions. *Calcified tissue international* 66(6):449-455.
61. Schenk R, Merz WA, Muhlbauer R, Russell RG, & Fleisch H (1973) Effect of ethane-1-hydroxy-1,1-diphosphonate (EHDP) and dichloromethylene diphosphonate (Cl 2 MDP) on the calcification and resorption of cartilage and bone in the tibial epiphysis and metaphysis of rats. *Calcif Tissue Res* 11(3):196-214.
62. Fleisch HA (1997) Bisphosphonates: preclinical aspects and use in osteoporosis. *Ann Med* 29(1):55-62.
63. Dorozhkin SV (2007) Calcium Orthophosphates. *J Mater Sci* (42):1061-1095.
64. Elliott JC (2002) Calcium phosphate biominerals. *Reviews in Mineralogy and Geochemistry* 48(1):427-453.
65. Glimcher MJ (1998) The nature of the mineral phase in bone: biological and clinical implications. *Metabolic bone disease and clinically related disorders,* (Academic Press, San Diego), pp 23-50.

Figure captions

Figure 1.
3D collagen-EV platform recapitulated microcalcifications seen in human atheroma. A) Schematic of assembly and use of 3D collagen platform. B) Scanning electron microscopy (SEM) image of a microcalcification formed in the 3D collagen platform after 8 days of incubation with calcifying EVs. C) Higher magnification view of yellow-outlined region in B. D) SEM image of calcified atherosclerotic plaque. E) Transmission electron microscopy (TEM) image of a microcalcification formed in the 3D collagen platform. F) TEM image of calcified atherosclerotic plaque.

Figure 2.
3D collagen-EV platform mediated the deposition of calcium phosphate mineral. A) Collagen hydrogel following 8 days of incubation with calcifying EVs, stained with a near-infrared fluorescent calcium tracer. B) Representative energy-dispersive spectroscopy (EDS) spectrum of a microcalcification in the 3D collagen platform. C) Microcalcification imaged in the 3D collagen platform using SEM. EDS was conducted for this microcalcification, yielding elemental maps of phosphorous, D, and calcium, E.

Figure 3.
EV-nucleated microcalcifications in 3D collagen platform were predicted to significantly increase fibrous cap tensile stress. A) Microcalcification imaged in the 3D collagen platform. A structure of identical dimensions as the microcalcification in *A* was added to a 3D simulation of an atheroma. Using this simulated atheroma, FEA of the fibrous cap under tensile stress was calculated, in which the simulated microcalcification was assigned material properties similar to those of the fibrous cap, B, or material properties of mineral, C. Elevated levels of tensile stress are indicated by bright colors (red), while baseline levels are indicated by cool colors (blue). D) Overlay of the SEM microcalcification image with the corresponding FEA predicted change in fibrous cap tensile stress.

Figure 4.
BiP reduced the maximum size and altered the morphology and elemental composition of calcific EV aggregates visualized via SEM. Collagen hydrogels were incubated with calcifying EVs and water (A, C) or BiP (ibandronate – B, D) for 8 days. BiP was added at day 0. Changes in microcalcification size can be seen at low magnification (A vs. B) and high magnification (C vs. D).

Figure 5.
The formation of microcalcifications varied significantly with single-dose BiP treatment in a time-dependent manner. A) Schematic depicting the experimental setup for treating samples with BiP at different times. B) Calcifying EVs were incubated in osteogenic medium for 8 days, and each sample was treated once with BiP, as depicted in *A*. After 8 days of incubation, the amount of calcium phosphate mineral formed was measured using a fluorescent-based assay.

Figure 6.
BiP treatment altered microcalcification morphology in a time-dependent manner. SEM (A-D) and AFM (E-H) were used to image microcalcifications formed in 3D collagen hydrogels that were treated at different times with a single dose of BiP, as depicted in Fig. 5*A*.

Figure 7.
BiP treatment altered the chemical composition of calcium phosphate mineral in a time-dependent manner. Calcifying EVs were incubated in osteogenic medium for 8 days, and each sample was treated once with BiP, as depicted in Fig. 5*A*. After 8 days of incubation, resultant calcium phosphate mineral was analyzed using FTIR.

Figure 8.
BiP treatment altered the predicted fibrous cap tensile stress attributed to single microcalcifications, in a time-dependent manner. Panels A-D demonstrate FEA analysis of the microcalcifications shown in Fig. 6*A-D*, respectively. The methodology behind FEA analysis was illustrated in Fig. 3. Panel E quantifies the average stress concentration factor for n=3 samples in the BiP treated groups, as compared to untreated microcalcifications (control). The groups were not statistically different from one another, as calculated using a one-way ANOVA with Tukey's Multiple Comparison's Test.

Figures

Figure 1A

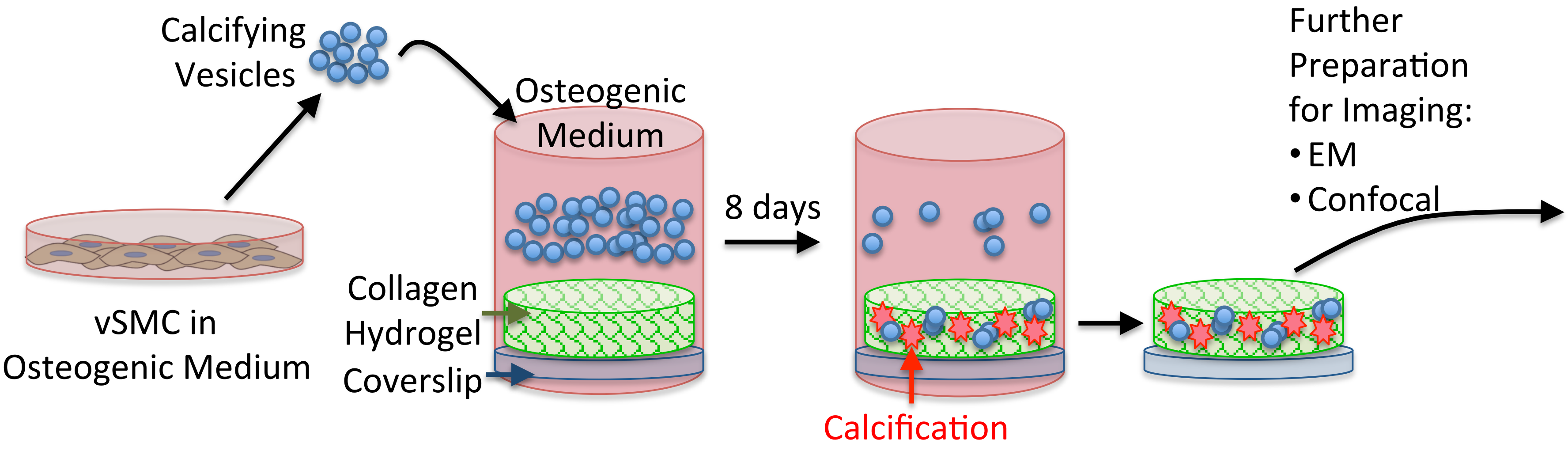
Calcifying
Vesicles
vSMC in
Osteogenic Medium
Osteogenic
Medium
Collagen
Hydrogel
Coverslip
8 days
Calcification
Further
Preparation
for Imaging:
• EM
• Confocal

Figure 1 B-F

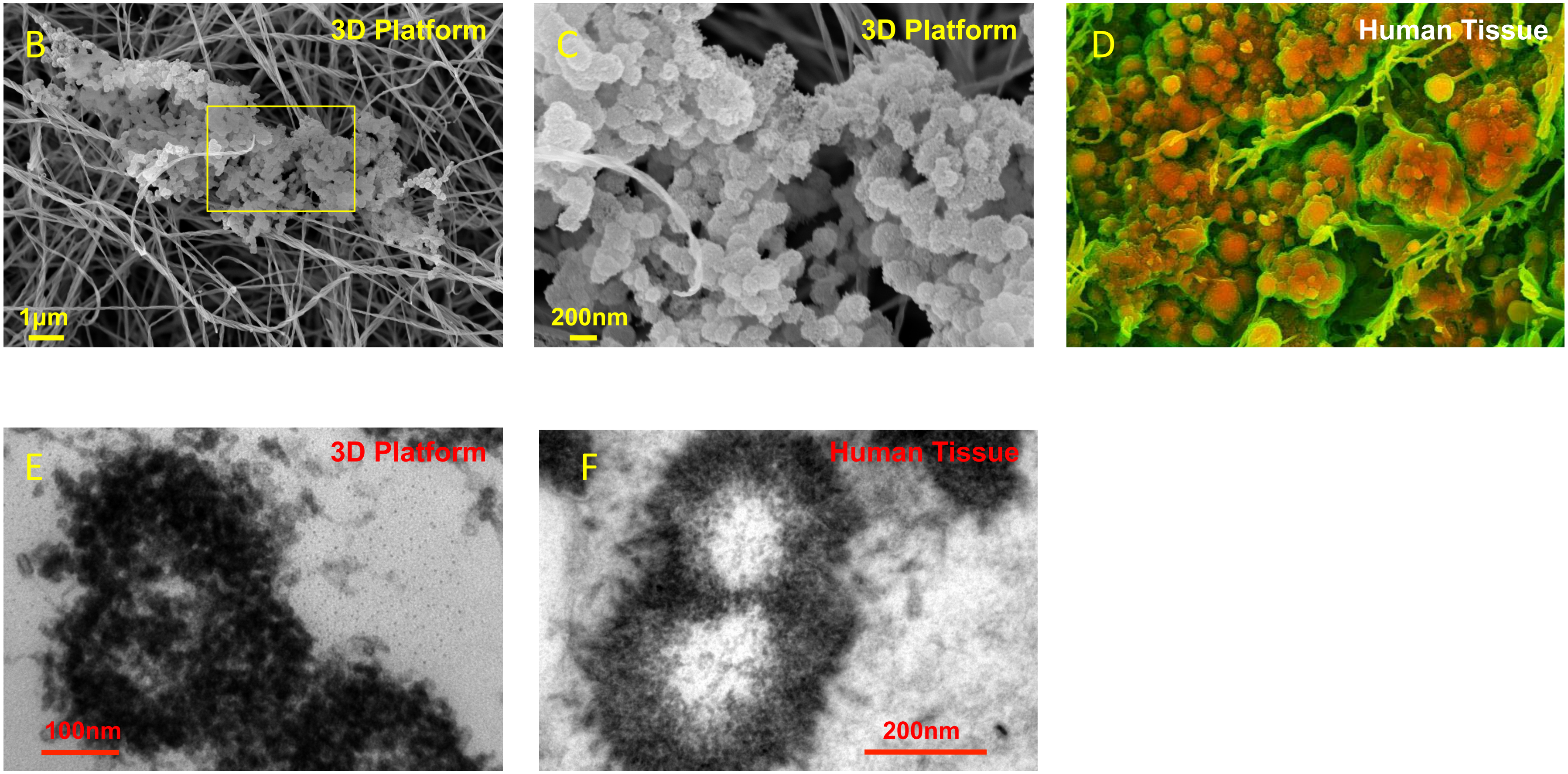
B
3D Platform
1μm
C
3D Platform
200nm
D
Human Tissue
E
3D Platform
100nm
F
Human Tissue
200nm

Figure 2

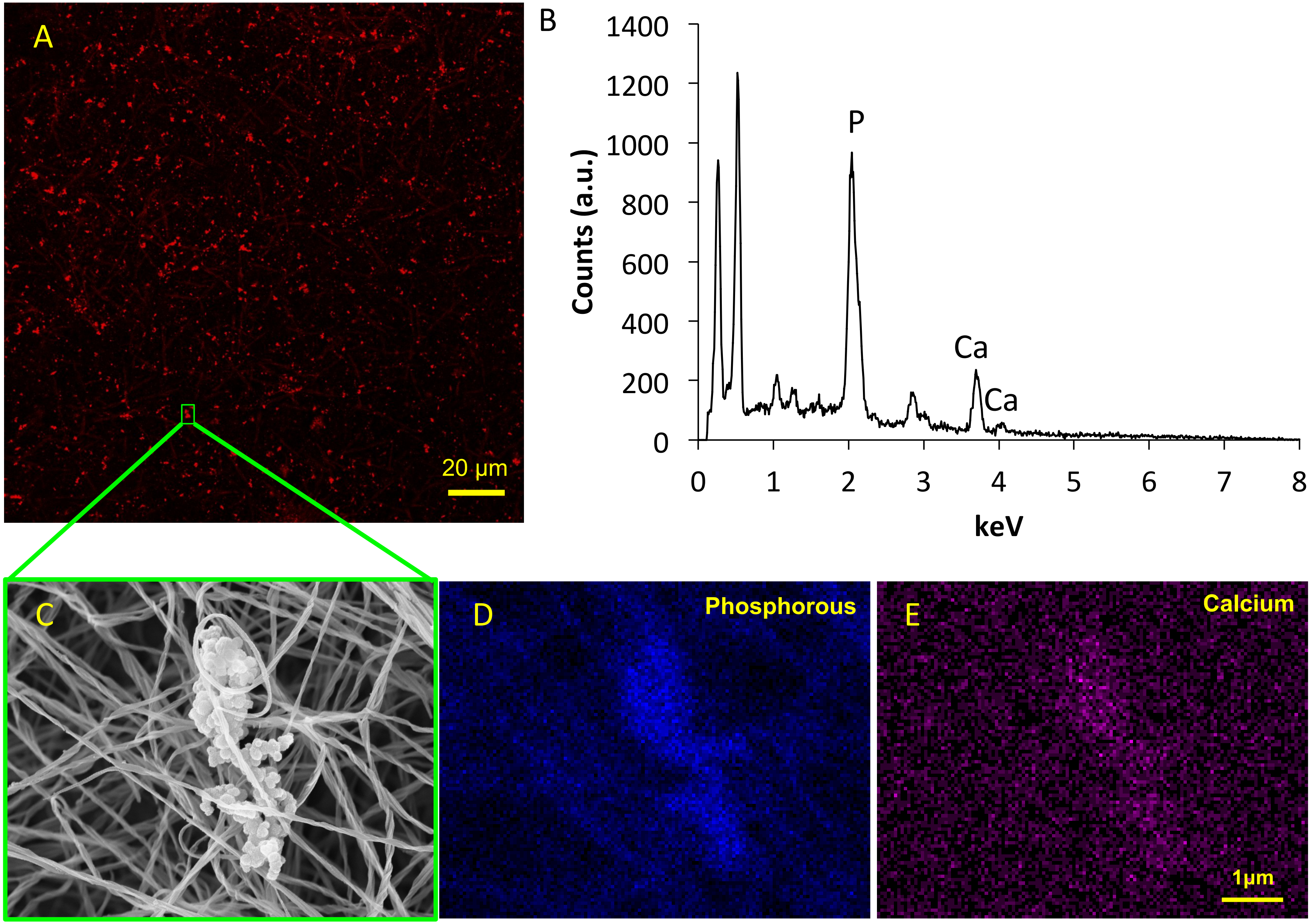
A
20 µm
B
Counts (a.u.)
1400
1200
1000
800
600
400
200
0
0
1
2
3
4
5
6
7
8
keV
P
Ca
Ca
C
D
Phosphorous
E
Calcium
1µm

Figure 3

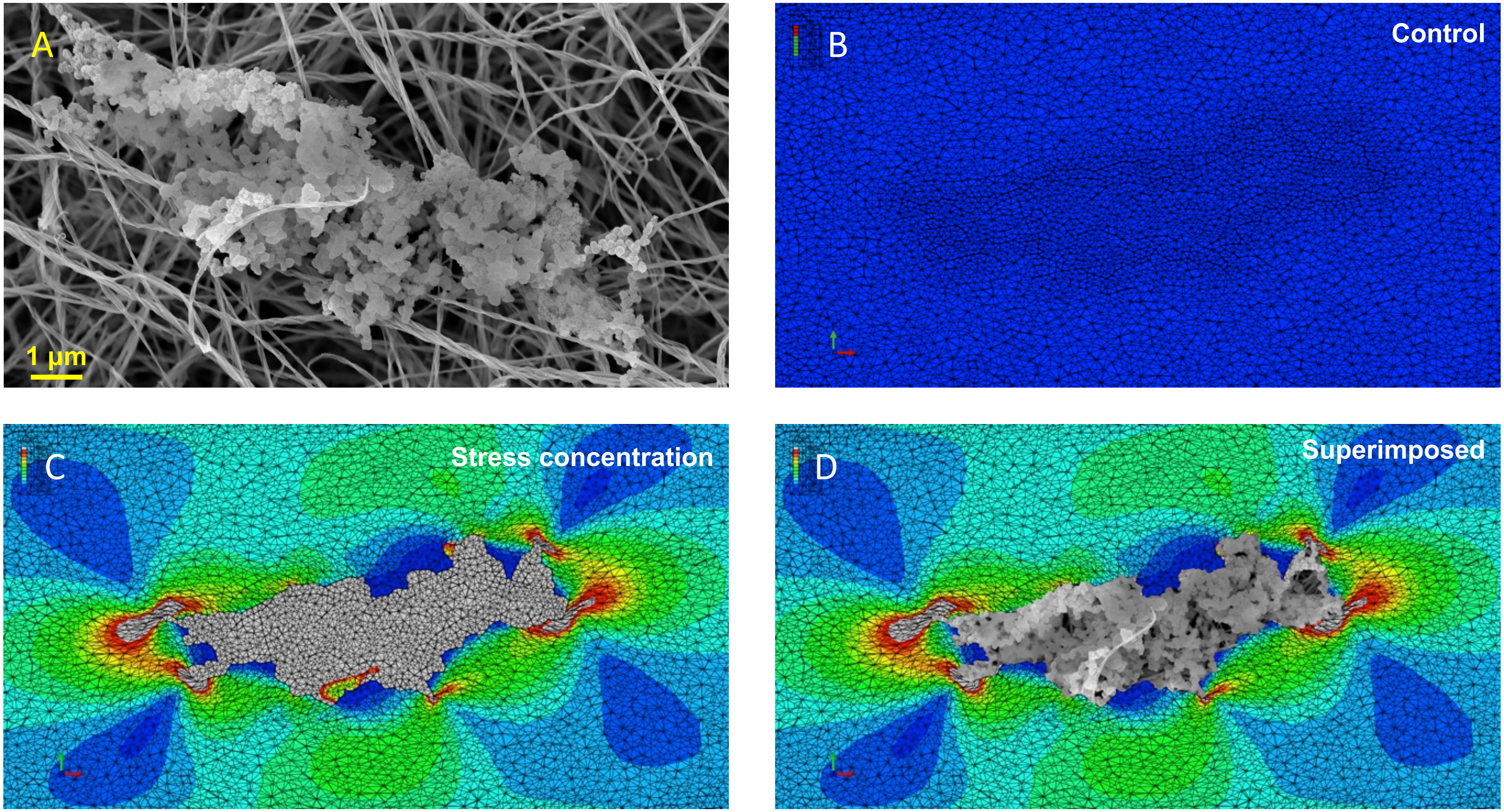
A
1 µm
B
Control
C
Stress concentration
D
Superimposed

Figure 4

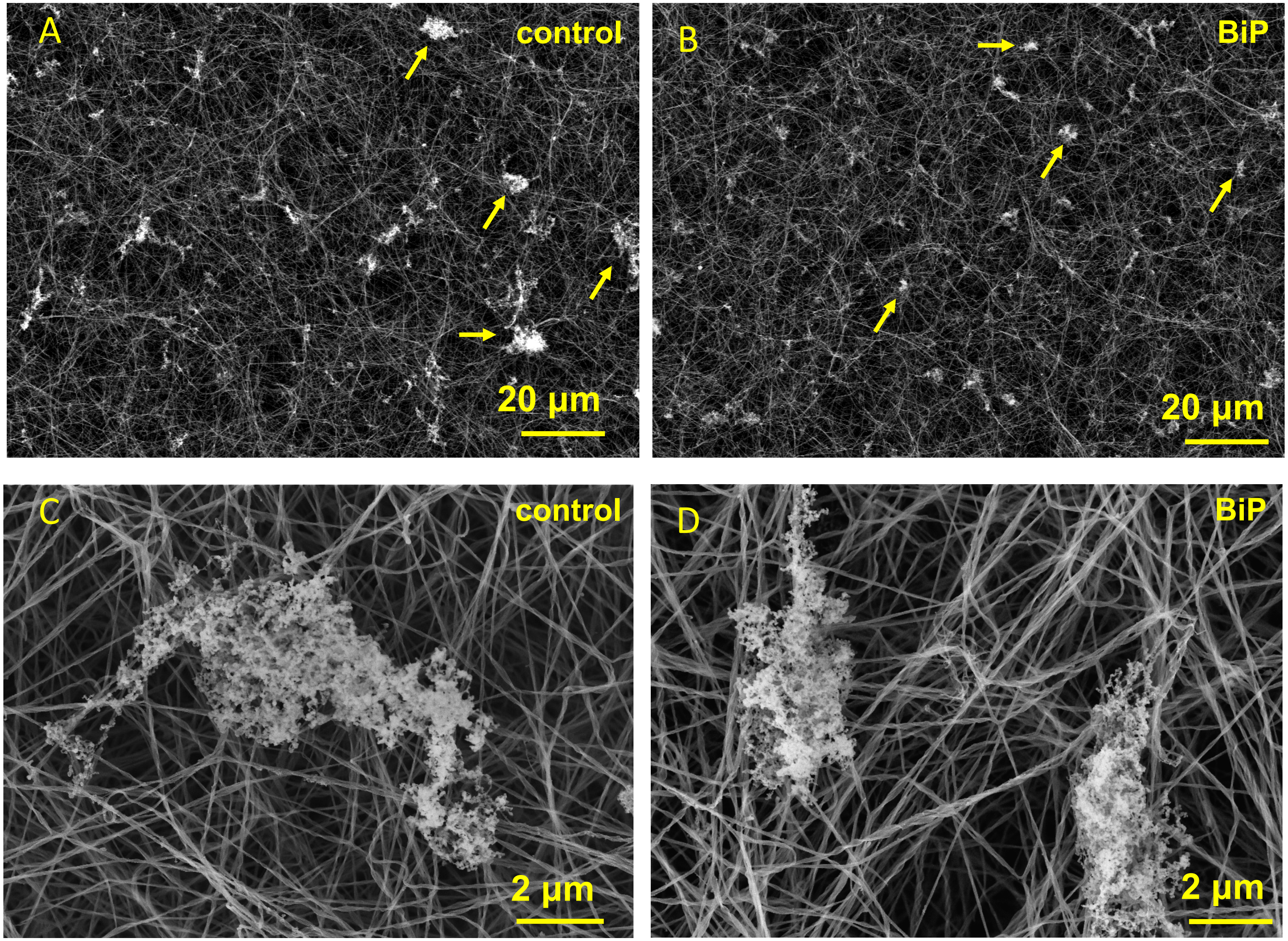

A
control
20 µm
B
BiP
20 µm
C
control
2 µm
D
BiP
2 µm

Figure 5A

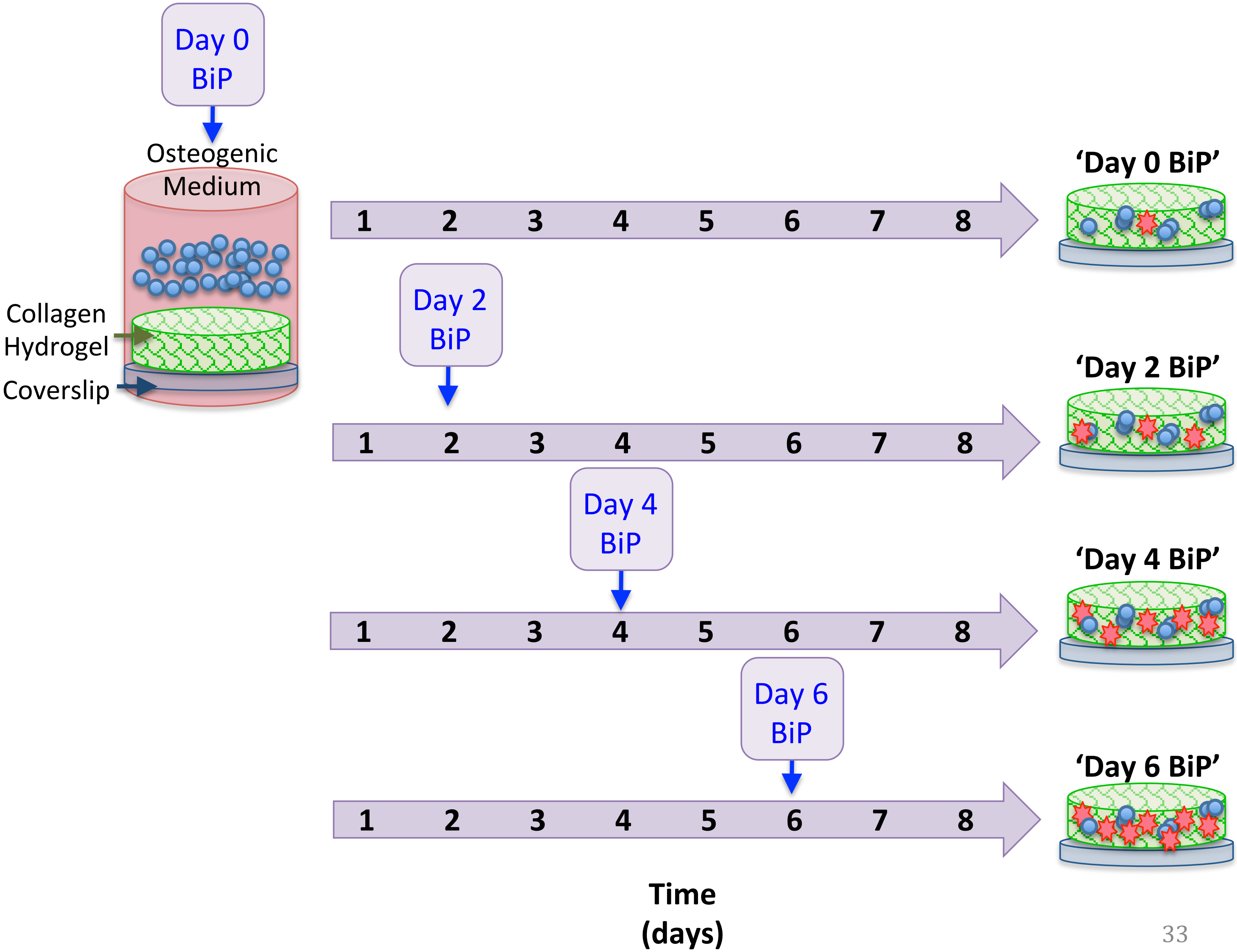
Day 0
BiP
Osteogenic
Medium
Collagen
Hydrogel
Coverslip
1 2 3 4 5 6 7 8
'Day 0 BiP'
Day 2
BiP
1 2 3 4 5 6 7 8
'Day 2 BiP'
Day 4
BiP
1 2 3 4 5 6 7 8
'Day 4 BiP'
Day 6
BiP
1 2 3 4 5 6 7 8
'Day 6 BiP'
Time
(days)

Figure 5B

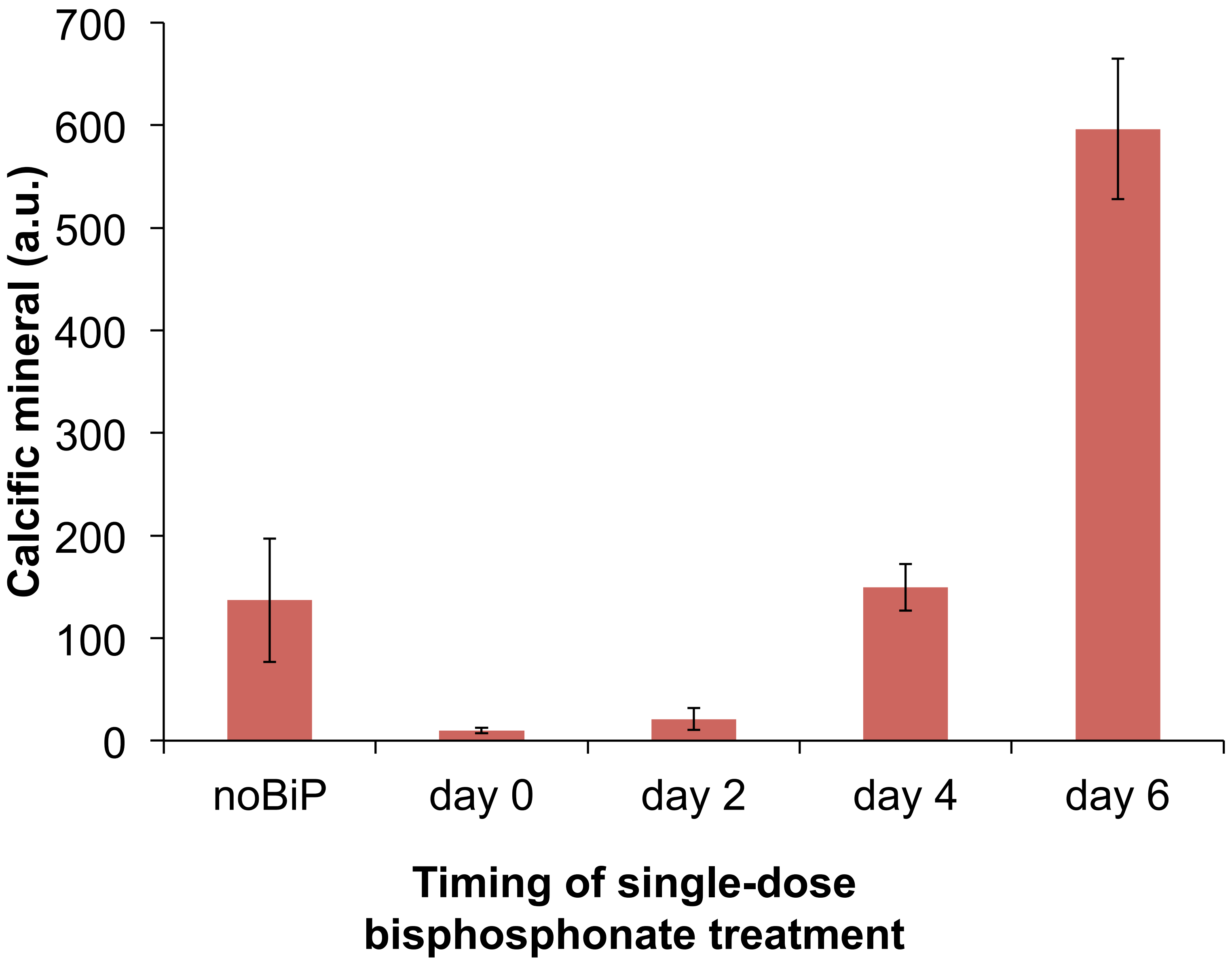
Calcific mineral (a.u.)
700
600
500
400
300
200
100
0
noBiP
day 0
day 2
day 4
day 6
Timing of single-dose bisphosphonate treatment

Figure 6

Scanning Electron Microscopy (SEM)

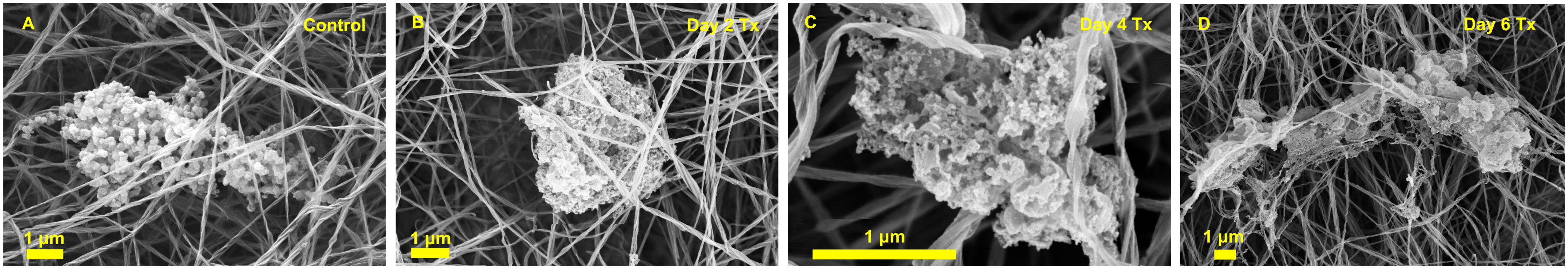
A
Control
1 µm
B
Day 2 Tx
1 µm
C
Day 4 Tx
1 µm
D
Day 6 Tx
1 µm

Atomic Force Microscopy (AFM)

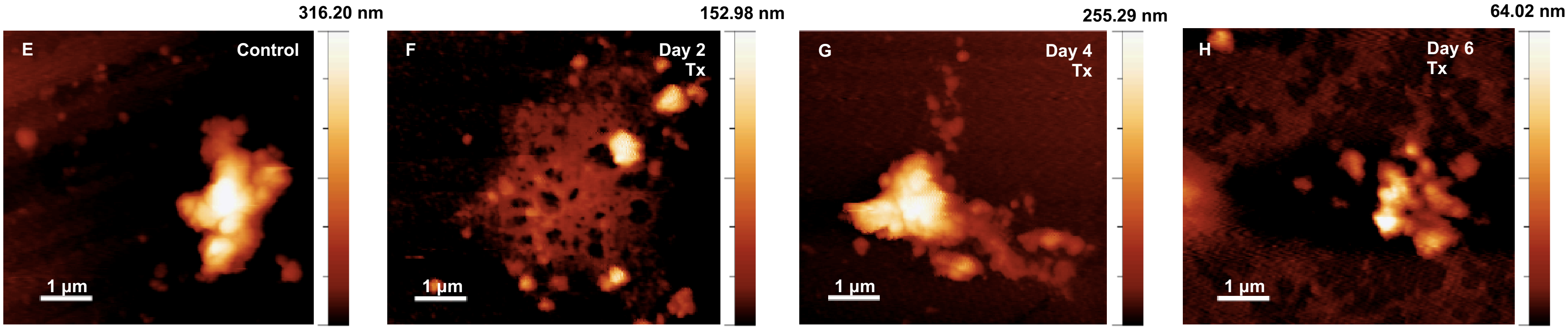
316.20 nm
E
Control
1 µm
152.98 nm
F
Day 2
Tx
1 µm
255.29 nm
G
Day 4
Tx
1 µm
64.02 nm
H
Day 6
Tx
1 µm

Figure 7

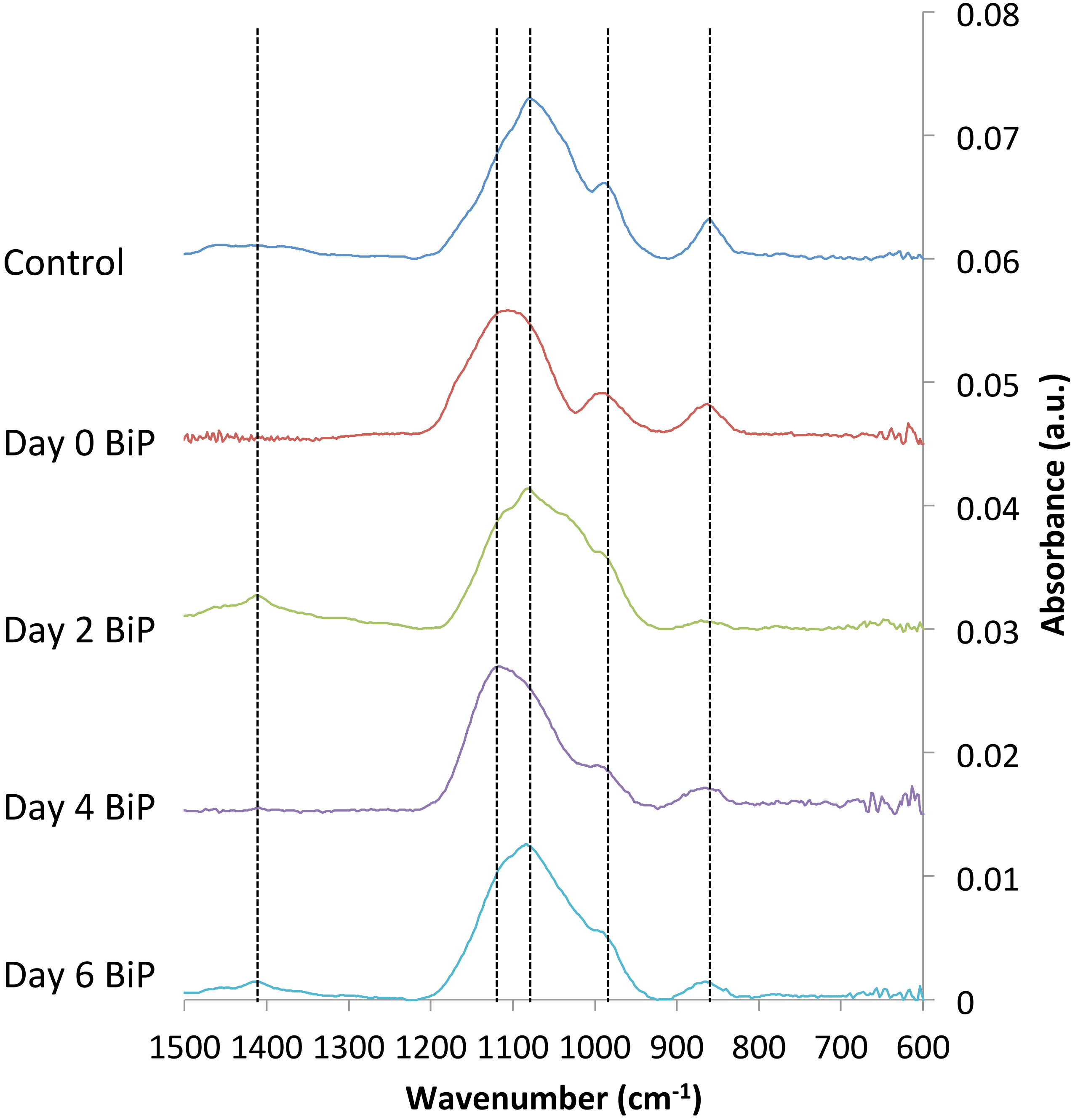
Control
Day 0 BiP
Day 2 BiP
Day 4 BiP
Day 6 BiP
0.08
0.07
0.06
0.05
0.04
0.03
0.02
0.01
0
Absorbance (a.u.)
1500
1400
1300
1200
1100
1000
900
800
700
600
Wavenumber (cm-1)

Figure 8

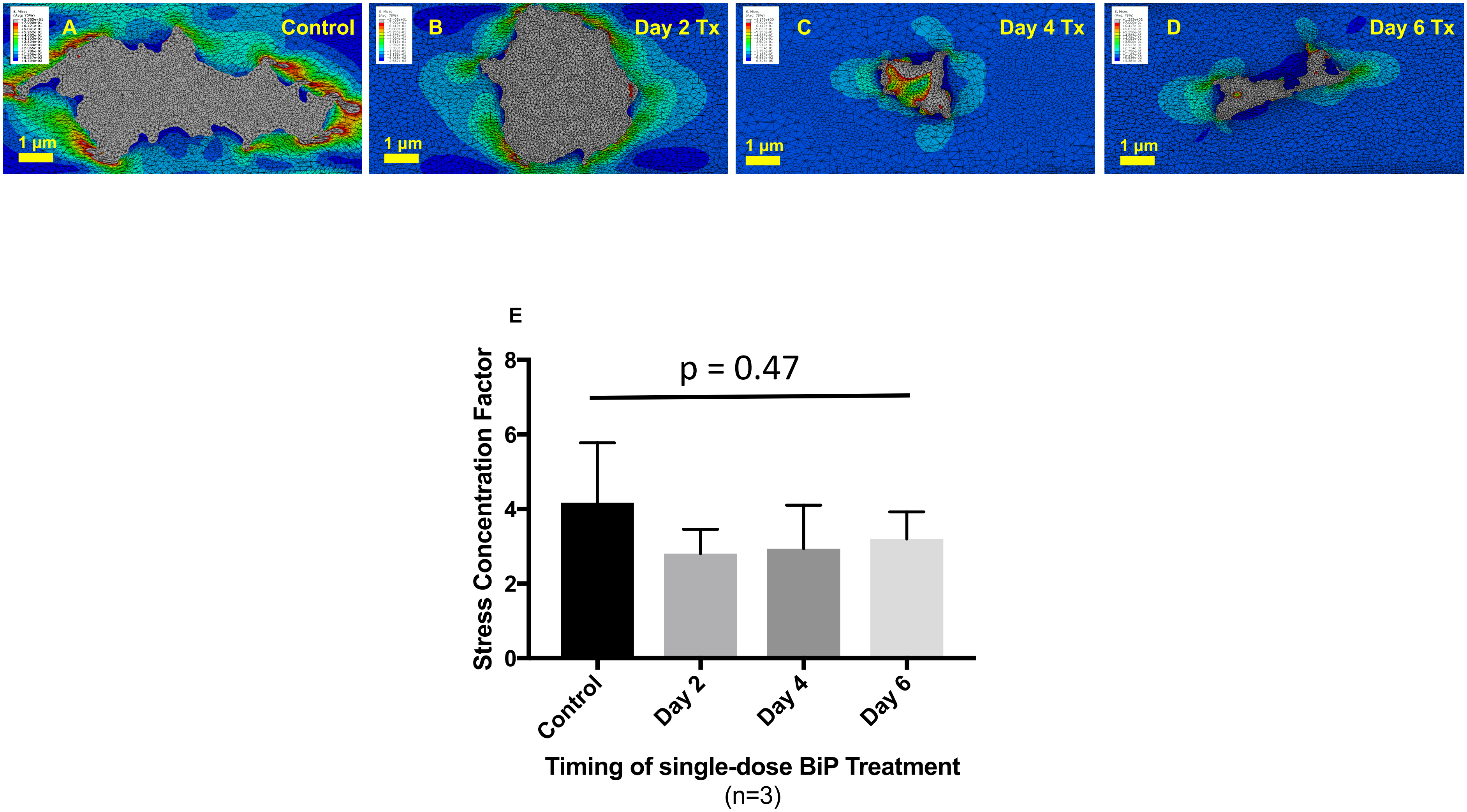
A
Control
1 µm
B
Day 2 Tx
1 µm
C
Day 4 Tx
1 µm
D
Day 6 Tx
1 µm
E
Stress Concentration Factor
8
6
4
2
0
p = 0.47
Control
Day 2
Day 4
Day 6
Timing of single-dose BiP Treatment
(n=3)